Authors

Mu, Changhua
Liu, Xiaoxi
Kim, Yaewon
et al.

Article

Clinically Translatable Hyperpolarized ^{13}C Bicarbonate pH Imaging Method for Use in Prostate Cancer

Changhua Mu, Xiaoxi Liu, Yaewon Kim, Andrew Riselli, David E. Korenchan, Robert A. Bok, Romelyn Delos Santos, Renuka Sriram, Hecong Qin, Hao Nguyen, Jeremy W. Gordon, James Slater, Peder E. Z. Larson, Daniel B. Vigneron, John Kurhanewicz, David M. Wilson, and Robert R. Flavell*

Read Online

ACCESS | Metrics & More | Article Recommendations | Supporting Information

ABSTRACT: Solid tumors such as prostate cancer (PCa) commonly develop an acidic microenvironment with pH 6.5−7.2, owing to heterogeneous perfusion, high metabolic activity, and rapid cell proliferation. In preclinical prostate cancer models, disease progression is associated with a decrease in tumor extracellular pH, suggesting that pH imaging may reflect an imaging biomarker to detect aggressive and high-risk disease. Therefore, we developed a hyperpolarized carbon-13 MRI method to image the tumor extracellular pH (pH$_e$) and prepared it for clinical translation for detection and risk stratification of PCa. This method relies on the rapid breakdown of hyperpolarized (HP) 1,2-glycerol carbonate (carbonyl-^{13}C) via base-catalyzed hydrolysis to produce HP ^{13}CO$_3$$^{2-}$, which is neutralized and converted to HP H^{13}CO$_3$$^-$. After injection, HP H^{13}CO$_3$$^-$ equilibrates with HP ^{13}CO$_2$ in vivo and enables the imaging of pH$_e$. Using insights gleaned from mechanistic studies performed in the hyperpolarized state, we solved issues of polarization loss during preparation in a clinical polarizer system. We successfully customized a reaction apparatus suitable for clinical application, developed clinical standard operating procedures, and validated the radiofrequency pulse sequence and imaging data acquisition with a wide range of animal models. The results demonstrated that we can routinely produce a highly polarized and safe HP H^{13}CO$_3$$^-$ contrast agent suitable for human injection. Preclinical imaging studies validated the reliability and accuracy of measuring acidification in healthy kidney and prostate tumor tissue. These methods were used to support an Investigational New Drug application to the U.S. Food and Drug Administration. This methodology is now ready to be implemented in human trials, with the ultimate goal of improving the management of PCa.
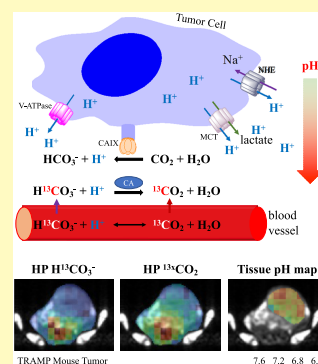
Prostate cancer (PCa) is a biologically heterogeneous disease with high morbidity and mortality. The American Cancer Society projected 288,300 PCa diagnoses and 34,700 PCa-related deaths in the United States in 2023.[1] PCa presents with a wide clinical spectrum, ranging from indolent tumors, which may never progress and require no treatment intervention, to highly aggressive malignancies, which will metastasize and ultimately lead to cancer-specific mortality.[2] Therefore, many methods, including blood-based biomarkers and advanced imaging techniques, have been developed for detecting aggressive PCa.[3−6]

The unconstrained proliferation, invasion, and therapeutic resistance of tumor cells are associated with the Warburg effect, which is indicative of an increased rate of glucose uptake, aerobic glycolysis, and lactic acid fermentation through the lactate dehydrogenase-catalyzed reaction.[7] The altered metabolic phenotypes include overexpression of monocarboxylate transporters, sodium−hydrogen exchanger isoform-1, vacuolar H$^+$-ATPase, and outward-facing carbonic anhydrase isoforms.[8,9] Consequently, tumors develop an acidic tumor microenviron-ment (TME) with extracellular pH (pH$_e$) of 6.5−7.2, in contrast to pH 7.4 in healthy tissue (Figure 1a).[10,11] The acidic TME is commonly associated with local invasion and metastasis in various cancers, including melanoma, breast, colon, renal, and prostate cancer, and leads to resistance to chemo-, immuno-, or radiotherapy.[12] Thus, extracellular acidosis of solid tumors represents a hallmark for cancer detection and treatment.[13−15]
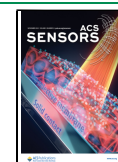
The ability to image tissue pH may facilitate detecting aggressive and potentially metastatic lesions and monitoring therapy response. Several advanced pH$_e$ imaging methods, including optical imaging, positron emission tomography, conventional ^{1}H, ^{19}F, ^{31}P, and CEST MRI, and electron
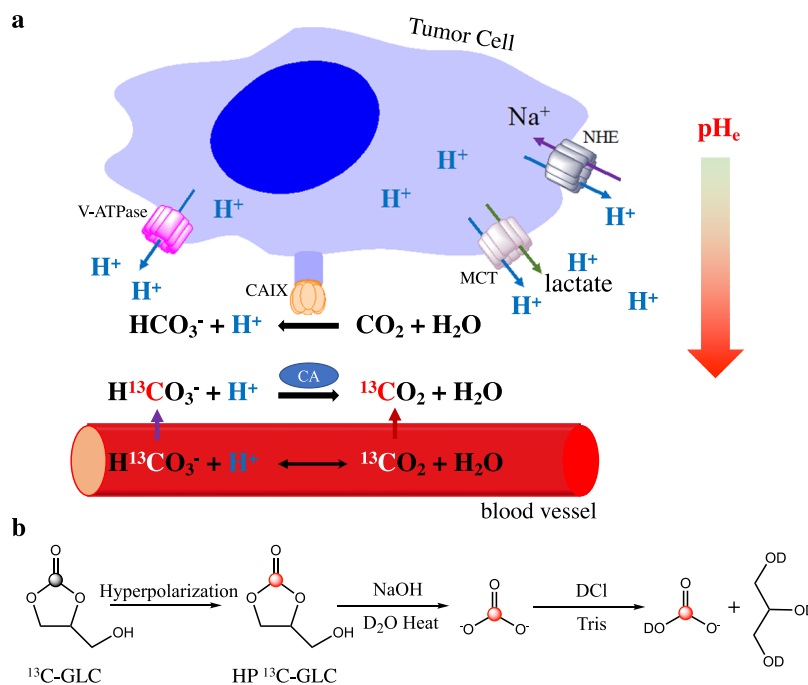
Figure 1. Hyperpolarized (HP) ^{13}C extracellular pH (pH$_e$) MRI imaging. (a) Extracellular acidification of the tumor microenvironment and the mechanism of imaging interstitial pH using hyperpolarized H^{13}CO$_3^-$. Note: NHE, Na$^+$/H$^+$ exchanger; MCT, monocarboxylate transporter; CAIX, carbonic anhydrase IX; LDH, lactate dehydrogenase; and V-ATPase, vacuolar H$^+$-ATPase. (b) Precursor strategy of polarizing ^{13}C-GLC and subsequent breakdown by NaOH to produce HP ^{13}CO$_3^{2-}$, which is neutralized and converted to HP H^{13}CO$_3^-$ by deuterium chloride (DCl) in the Tris buffer system. Glycerol is a biocompatible side product of the hydrolysis of ^{13}C-GLC. Note: the position of the ^{13}C label is indicated with a black circle for the thermal equilibrium state and red for the hyperpolarized state.

paramagnetic resonance, have been developed.[9,15] On the other hand, intracellular pH (pH$_i$) change also reflects the metabolic states of cancer cells in tumor growth and dissemination.[12] This can be measured *in vivo* using techniques including phosphorus NMR and others,[16] and more recently, genetically encoded sensors have been developed for using fluorescence lifetime imaging to study pH$_i$ under a microscope.[17] Due to various potential issues, including limited penetration depth, radiation risks, low sensitivity, and limited spatiotemporal resolution, none of these methods have found widespread clinical use.[9,15] Thus, there is a substantial clinical need for developing an accurate and noninvasive pH imaging method for routine clinical applications. In pioneering studies, Gallagher et al. described the hyperpolarization (HP) of H^{13}CO$_3^-$ using dynamic nuclear polarization and its application to tumor pH$_e$ imaging.[18] However, the low concentration (~100 mM), potential toxicity of the CsH^{13}CO$_3$ formula, and low polarization level (~16% at 9.4 T at the start of dissolution) are primary obstacles that discourage the feasibility of clinical application.[19] To overcome the limitations of the originally described methodology, researchers have explored precursor strategies that involve a mechanism to breakdown a highly polarized nontoxic organic compound to produce desired HP H^{13}CO$_3^-$. For instance, Rizi et al. reported the rapid decarboxylation of an α-keto carboxylic acid with H$_2$O$_2$, which realized multimetabolite imaging and simultaneously produced a combined concentration of 64 mM HP H^{13}CO$_3^-$ and HP ^{13}CO$_2$ without loss of polarization (~16%) for pH$_e$ imaging.[20] We reported another precursor strategy that relies on the breakdown of HP [1-^{13}C]1,2-glycerol carbonate (^{13}C-GLC) to liberate HP ^{13}CO$_3^{2-}$ via a hydrolysis reaction catalyzed by NaOH, followed by neutralization and conversion to the desired probe HP H^{13}CO$_3^-$ with a polarization level of 16.4 ± 1.3%

(Figure 1b).[21] Moreover, we observed tumoral acidification accompanying disease progression in the transgenic adenocarcinoma of the prostate (TRAMP) mouse model.[22] Taken together, these prior publications suggested that HP H^{13}CO$_3^-$ is an endogenous probe that exhibits promise for clinical translation in imaging tumor pH$_e$.[18,21−24]

The most widely studied probe, HP [1-^{13}C] pyruvate, has been employed for imaging tumor metabolism in patients diagnosed with PCa.[25] More recently, copolarized [1-^{13}C] pyruvate and [^{13}C, ^{15}N$_2$] urea enabled simultaneous metabolic and perfusion imaging in patients.[26,27] However, compared to theses clinical probes, producing highly polarized and human-injectable H^{13}CO$_3^-$ solutions poses a substantial challenge due to the complexity and time sensitivity of postdissolution manipulations, akin to preparing short-lived radiopharmaceuticals.

In this work, we report the development of a highly optimized HP H^{13}CO$_3^-$ tissue pH imaging method that is suitable for clinical studies. We found that our prior method, which had shown promise in preclinical studies, encountered challenges when transitioning to the clinical 5T GE SpinLab polarizer system, including a profound loss of polarization and imaging signals. Thus, we performed detailed chemical mechanistic studies in both thermal equilibrium and hyperpolarized states, which informed a new method to retain polarization after dissolution. To enable the postdissolution preparation of HP H^{13}CO$_3^-$ from HP ^{13}C-GLC, we customized a reaction apparatus that is suitable for clinical use following Good Manufacturing Practice (GMP) standards. We validated this method using a specially designed radiofrequency pulse sequence on a GE 3T clinical MRI scanner in several murine models including clinically relevant PCa models. These data were used to support the Investigational New Drug (IND)

application to the U.S. Drug and Food Administration (FDA), and we received a notification that our study may proceed. Future directions include conducting clinical studies in patients with PCa to determine the feasibility of using this method for early detection of aggressive PCa, risk stratification, and monitoring therapy response.

◼ EXPERIMENTAL SECTION

NMR Characterization of the NaOH-Catalyzed ^{13}C-GLC Hydrolysis Reaction. *Reaction Endpoint Study: Titration of ^{13}C-GLC with NaOH.* A mixture of ^{13}C-GLC (11.8 mg or 0.1 mmol), 0−1.5 equiv (in 0.5 equiv increments) of NaOH, and a small amount of [^{13}C, ^{15}N$_2$] urea as an internal reference in 500 μL of deuterium oxide (D$_2$O) was loaded to an NMR tube, incubated in a hot water bath set at 80 °C for 1 min, and then cooled down quickly in a room-temperature water bath for 10 s. ^{1}H NMR and ^{13}C NMR spectra of the sample were acquired immediately with a preset NMR spectrometer (Bruker Advance III HD 400) with approximately 2 and 5 min data acquisition time, respectively (Page S3). Similarly, the experiment was repeated with a smaller increment (0.1 equiv) of NaOH from 1.0 to 1.4 equiv. The same settings were also used in other ^{13}C NMR acquisition steps in Figures 3c, S1, S3, and S6−S10.

Kinetic Study of ^{13}C-GLC Hydrolysis. ^{13}C-GLC (11.8 mg or 0.1 mmol) solution (200 μL) and NaOH solution (300 μL) with 0.5, 1.0, 2.0, or 3.0 equiv in D$_2$O were prewarmed to 60 °C. They were mixed in an NMR tube and immediately loaded for ^{1}H NMR data acquisition in a preset 500 MHz Varian INOVA NMR spectrometer (Agilent Technologies, Palo Alto, CA) equipped with a 5 mm triple-tuned, ^{13}C direct-detect, triple-axis gradient-equipped broadband probe (Agilent Technologies) with the temperature regulated at 50 °C. ^{1}H NMR spectra were collected every 5 s for 70 s (Page S3). The ^{1}H NMR data were processed and fitted using MestreNova software 14.2 by tracking the signal intensity (integrals) decrease of ^{13}C-GLC and increase of glycerol during the reaction.[28,29]

Preparation and Hyperpolarization of the ^{13}C-GLC Formulation. The ^{13}C-GLC formulation for hyperpolarization was prepared by mixing ^{13}C-GLC with 15 mM trityl radical AH111501 sodium. In polarization characterizations and *in vivo* studies, 200 mg of the mixture of ^{13}C-GLC/trityl radical was polarized using a GE 5T SPINlab polarizer (GE Healthcare, Waukesha, WI) at 0.8 K for ~7 h and dissolved in 15 mL of a preheated aqueous solvent, yielding 8.5 mL of an HP ^{13}C-GLC solution (~200 mM). In clinical full-scale verification studies, 780 mg of the mixture was polarized and dissolved in 35 mL of a preheated aqueous solvent, yielding 28.5 mL of an HP ^{13}C-GLC solution (~230 mM).

Polarization Characterization. A 1.4 T benchtop NMR spectrometer (Pulsar, Oxford Instruments, Oxford, U.K.) was used to acquire the ^{1}H decoupled ^{13}C NMR spectra of both the real-time decay of hyperpolarized ^{13}C signals and the average of fully relaxed ^{13}C signals in the thermal state for characterizing the polarization properties, including the degree of polarization and the time constant of the polarization decay (T_1). The following parameters were set for the HP acquisition: 5° flip angle, 8000 Hz spectral width, 0.125 Hz spectral resolution, 4.5 s temporal resolution, and a total of 100 repetitions. After the HP acquisition, 1% v/v Gd-DTPA (Magnevist, Bayer, Whippany, NJ) was added to reduce T_1 for expediting the NMR data acquisition at thermal equilibrium. It was quantified with the following parameters: 14 s relaxation delay to fully relax ^{13}C spins, 90° flip angle, and 1000 averages. T_1 values of HP H^{13}CO$_3^-$ and ^{13}CO$_2$ were estimated from their HP signal decays after correction for the loss of magnetization due to RF excitation. To prevent the escape of HP ^{13}CO$_2$, except when adding Gd-DTPA, the NMR tube was continuously sealed. The solution state polarization (%Pol) was estimated from the comparison of the intensity of the signal on the first HP spectrum to that of the ^{13}C thermal equilibrium (ThE) spectrum.

%Pol = enhancement factor × ThE polarization

where enhancement factor = HP signal intensity/ThE signal intensity/ sin(α), where α is the flip angle.

ThE polarization (P_{ThE}) is determined by Boltzmann's law

$$P_{ThE} = \frac{n_+ - n_-}{n_+ + n_-} = \tanh\left(\frac{\hbar\gamma B_0}{2k_B T}\right)$$

where $\hbar$ is the Planck constant (6.626 × 10^{-34} J/Hz), γ is the gyromagnetic ratio of carbon-13 (10.705 × 10^6 Hz/T), B_0 is the magnetic field in tesla (T), k_B is the Boltzmann constant (1.38 × 10^{-23} J/K), and T is the temperature in kelvin (K).

Toxicology Study. Three male Sprague−Dawley rats (4−5 months old, 0.45−0.50 kg body weight) were used for the toxicity studies. The HP H^{13}CO$_3^-$ solution (2.5 mL) produced following the clinical SOP was injected intravenously into each rat via the tail vein. The rats' vital signs, including heart rate, respiratory rate, and oxygen saturation, were recorded using a pulse oximeter (MouseOx; Starr Life Sciences Corp, Oakmont, PA) 5 min before, during, and 20 min after injections. Three blood samples of each rat were collected at the time points of 10 min before injection, 20 min after injection, and 2 weeks after injection for the complete blood counts and liver−kidney function laboratory tests conducted in the Comparative Pathology Laboratory, School of Veterinary Medicine, University of California, Davis. Meanwhile, their body weights were monitored every 3 days, and necropsy and gross pathological examinations were performed 2 weeks after injections.

Preparation of Animal Models for HP ^{13}C pH$_e$ MRI Imaging Studies. All animal studies were conducted in compliance with a protocol approved by the Institutional Animal Care and Use Committee (IACUC) at the University of California, San Francisco. Healthy Sprague−Dawley rats (18−22 weeks old, 0.45−0.50 kg body weight) were purchased from Taconic Biosciences. TRAMP mice were acquired from Roswell Park Cancer Institute (Buffalo, NY) and raised for about 6 months. The tumor volume was monitored by a 3T Bruker ^{1}H MRI imaging system weekly until it reached 2 cm^3 for HP ^{13}C pH$_e$ MRI imaging studies to be started.

Two cohorts of three patient-derived xenograft (PDX) mice models were prepared by implanting LTL-545 and LuCaP 93 cells in the livers of NSG strain mice (6−8 weeks old, 24−30 g body weight). Briefly, a small (1−2 cm) incision was made on the abdomen of the mouse to expose the liver, and approximately 5−6 million PCa cells in phosphate-buffered saline solution loaded in an insulin syringe were injected. The wound was sutured-closed. Tumor growth was monitored by a 3T Bruker ^{1}H MRI imaging system weekly after 8 weeks of surgery until it reached 2 cm^3 for HP ^{13}C pH$_e$ MRI imaging studies.

***In Vivo* Hyperpolarized ^{13}C MRI pH$_e$ Imaging Studies.** HP ^{13}C *in vivo* imaging data were acquired by a ^{1}H/^{13}C transceiver single-channel birdcage coil on a GE 3T clinical MRI scanner. The HP H^{13}CO$_3^-$ formula was injected via the tail vein (1.5 mL for rats and 200 μL for mice) in 12 s, and dynamic metabolite-specific imaging was automatically triggered in 3 s when the HP bolus of the injection reached the region of interest with an autonomous scanning protocol, including real-time frequency calibration for H^{13}CO$_3^-$ signals and B$_1$ field calibration implemented on the RTHawk platform (HeartVista, Los Alto, CA).[30] HP H^{13}CO$_3^-$ and HP ^{13}CO$_2$ signals were acquired using a metabolite-specific 2D gradient echo (GRE) sequence[26,27,31,32] equipped with flow suppression gradients[33] for eliminating the interference from the strong signal of HP H^{13}CO$_3^-$ accumulated in the artery. The design parameters include a spectral-spatial excitation pulse with a 100 Hz passband, 6.63 ms pulse duration, and single-shot spiral gradients with a 25 ms readout duration and spoiler gradients.[34] The acquisition parameters include flip angles of 45° for HP ^{13}CO$_2$ and 10° for HP H^{13}CO$_3^-$, a spatial resolution of 2.5 × 2.5 × 20 mm^3, a flow suppression gradient b value of 23 (rat) or 50 (mouse) s/mm^2, an echo time of 14 (rat) or16.8 (mouse) ms, a repetition time of 80 (rat) or 85 (mouse) ms, single slice, a temporal resolution of 0.4 s, and a total of 90 time points. At each acquisition time point, the HP ^{13}CO$_2$ data were acquired prior to HP H^{13}CO$_3^-$ data with 0.2 s/metabolite (temporal resolution = 0.4 s) for minimizing residual magnetization from the former excitation. The imaged pH value was generated using a modified Henderson−Hasselbalch equation, with pK_a = 6.1 at 37 °C.[21]
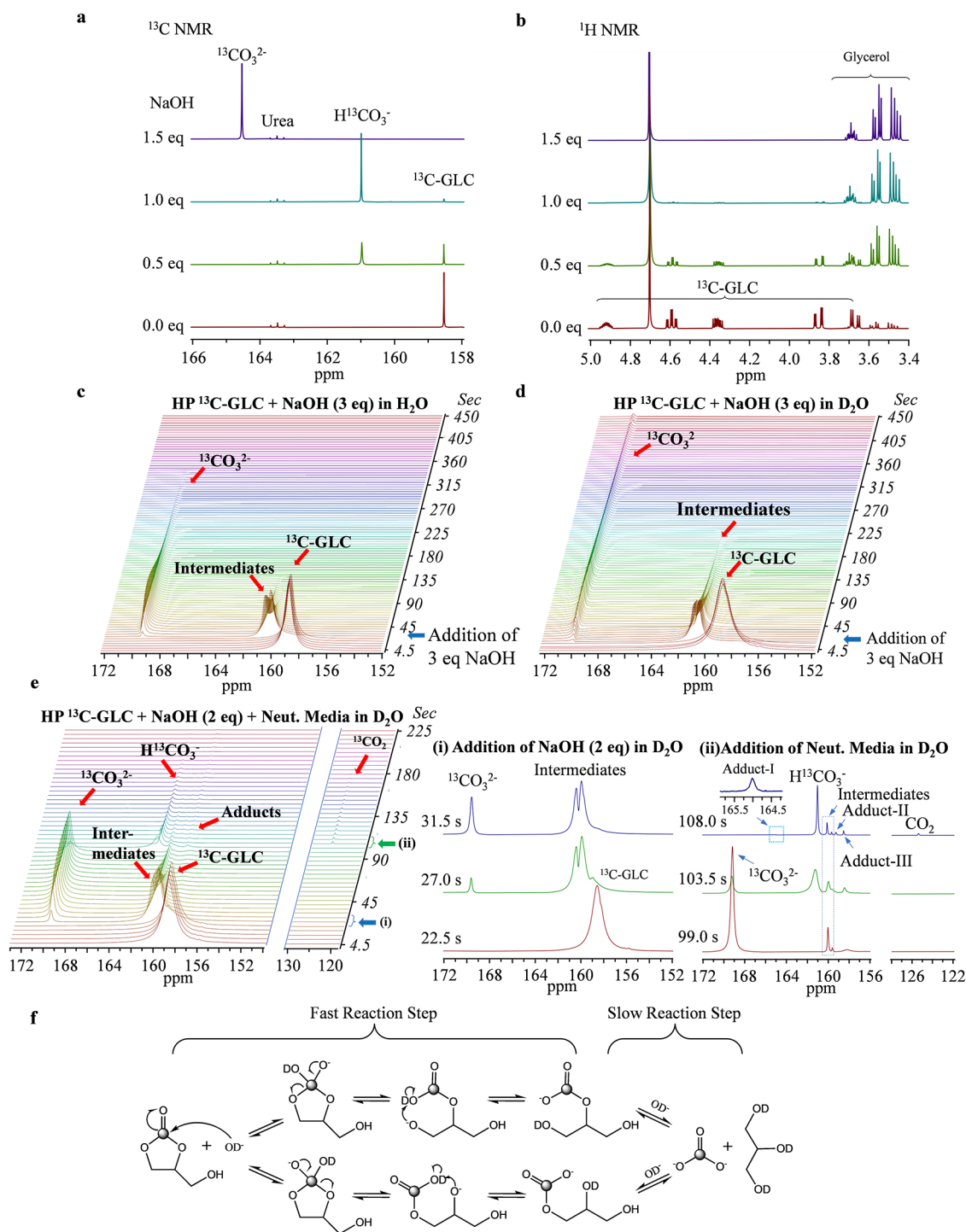
Figure 2. Investigation of the GLC hydrolysis and neutralization procedures by NMR spectroscopy at the thermal equilibrium and hyperpolarized (HP) states. (a, b) Thermal-state reaction endpoint studies: ^{13}C-GLC hydrolysis reaction at 80 °C in the presence of 0−1.5 eq. of NaOH in 500 μL of D$_2$O for 1 min before (a) ^{13}C and (b) ^{1}H NMR acquisition steps. (c−e) HP ^{13}C-GLC reaction kinetics studies in an NMR tube inserted in a 1.4 T portable NMR spectrometer with a temporal resolution of 4.5 s and a flip angle of 5°: addition of 3 equiv of NaOH to HP ^{13}C-GLC in (c) H$_2$O and (d) D$_2$O with identical signals HP CO$_3^{2-}$ (169.2 ppm), two intermediates from the ring-opening from each side of HP ^{13}C-GLC (160.1 and 159.7 ppm), and (e) addition of 2 equiv of NaOH (i), followed by 3 equiv of 1.5 M molar equivalent mixture of Tris and DCl (ii). Notes: (1) Table 2 summarizes the T_1 values of all of the HP ^{13}C-GLC hydrolytic products; (2) adduct I = Tris−^{13}CO$_3^{2-}$ (165.0 ppm), adduct II = glycerol−H^{13}CO$_3^-$ (159.3 ppm), and adduct III = Tris−H^{13}CO$_3^-$ (158.6 ppm). (f) Proposed reaction mechanism of hyperpolarized ^{13}C-GLC hydrolysis catalyzed by NaOH in D$_2$O.

$$pH = pK_a + \log\left[\frac{S_{HCO_3^-}}{S_{CO_2}} \times \frac{\sin \alpha_{CO_2}}{\sin \alpha_{HCO_3^-}}\right]$$

where S is the signal intensity and α is the flip angle.

The pH values were presented as means within the region of interest, while their associated uncertainties were determined by analyzing the noise levels in the background compared to the intensities of HP H^{13}CO$_3^-$ and HP ^{13}CO$_2$ signals, enabling evaluation of the extent to which noise affected the accuracy of pH imaging. The regions either

outside the animal body or with a low signal-to-noise ratio (SNR) were masked to exclude spurious values.

After imaging, we kept the animal under anesthesia, made an incision to access the tumor, and used a calibrated microelectrode pH meter (Oakton Instruments, pH 6+) to assess the tumor pH at three different locations and validate the accuracy of the imaging measurement.

■ RESULTS

Characterization of ^{13}C-GLC Hydrolysis at Thermal Equilibrium. To study the reaction kinetics and mechanism of ^{13}C-GLC breakdown, we used single-time point ^{1}H and ^{13}C NMR and dynamic multitime point ^{1}H NMR at thermal equilibrium.

We incubated ^{13}C-GLC with varying amounts of NaOH in D$_2$O at 80 °C (500 μL) for 1 min and acquired the single-time point ^{13}C NMR and ^{1}H NMR spectra (Figure 2a,b). In both spectra, we identified the ^{13}C-GLC resonances[35] and observed their decrease with addition of NaOH. We also observed a concomitant increase in its hydrolytic products—glycerol in ^{1}H NMR spectra and a signal shifting from 161.2 to 164.8 ppm in ^{13}C NMR spectra, which is assignable to the pH-dependent equilibrium of H^{13}CO$_3^-$ and ^{13}CO$_3^{2-}$. Due to the rapid exchange of protons between H^{13}CO$_3^-$ and ^{13}CO$_3^{2-}$ in the NMR time scale in an alkaline solution, the observed ^{13}C chemical shift of the carboxyl group can be expressed as a weighted average of the ^{13}C chemical shift between them, resulting in only one single resonance in ^{13}C NMR spectra.[36] Thus, the signal assignments of H^{13}CO$_3^-$ and ^{13}CO$_3^{2-}$ in this context implicate only the dominant component at a given pH rather than the distinct chemical species. We did not observe additional signals arising from the possible intermediate species resulting from the ring-opening hydrolysis of ^{13}C-GLC from each side. We found that a slight excess of NaOH (1.3 equiv) was required to ensure a complete breakdown of ^{13}C-GLC (Figure S1).

We then acquired dynamic ^{1}H NMR spectra every 5 s for 2 min at 50 °C to monitor time-dependent ^{13}C-GLC breakdown with addition of 1.0–3.0 equiv of NaOH. We identified and monitored the changes in ^{13}C-GLC and glycerol resonances. The spectra revealed that increasing NaOH up to 2.0 equiv led to a faster ^{13}C-GLC breakdown rate, and no intermediates were detected (Figure S2).

Investigation of Hyperpolarized ^{13}C-GLC Hydrolysis. The representative results of the HP ^{13}C-GLC hydrolysis experiments are summarized in Table 1. The precursor HP ^{13}C-GLC, similar to HP ^{13}C-pyruvate,[25,27] produced a highly polarized aqueous solution (51.2% measured at 35 s after dissolution) with a long T_1 (104.5 s) at 1.4 T (Trial 1). However, there was a substantial loss of polarization on the hydrolytic product ^{13}CO$_3^{2-}$ after the addition of NaOH (Trials 2 and 3). Prior studies have suggested that deuterium oxide (D$_2$O) solvation of HP ^{13}C molecules containing exchangeable protons can extend the lifetime of hyperpolarization by reducing dipolar relaxation via proton–deuterium exchange.[37] We therefore dissolved HP ^{13}C-GLC in D$_2$O (Trial 4) and found that T_1 increased to 163.3 s from 104.5 s in H$_2$O (Trial 1). Furthermore, we repeated the hydrolysis but used D$_2$O for dissolution in Trial 5. This change markedly increased the polarization level of ^{13}CO$_3^{2-}$ to 49.9% at 48 s after dissolution with a long T_1 (150.2 s).

To elucidate the mechanism of GLC hydrolysis, we monitored the reaction by transferring HP ^{13}C-GLC dissolved in either H$_2$O or D$_2$O to an NMR tube loaded in the 1.4 T NMR

Table 1. HP ^{13}C-GLC Hydrolysis with NaOH to Produce HP Carbonate in H$_2$O and D$_2$O[a]

trial no.	solvent	NaOH (equiv)	time after dissolution (s)	T_1 at 1.4 T (s)	%Pol of the first spectrum	pH or pH*
1[§]	H$_2$O		35	104.5	51.2	6.55
2	H$_2$O	1.5	49		<1.0	9.46
3	H$_2$O	3.0	48	51.0	4.8	12.85
4[§]	D$_2$O		37	163.3	59.5	6.51
5	D$_2$O	3.0	48	150.2	49.9	12.94
6	D$_2$O	2.0	42	143.3	51.3	11.06
7	D$_2$O	1.5	54	139.5	44.5	9.88

[a](1) The polarization time of ^{13}C-GLC was ~7 h, which corresponded to five times the time constant of solid-state hyperpolarization buildup to suffice the subsequent studies. (2) [§]Trials 1 and 4 did not include NaOH to study the polarization properties of HP ^{13}C-GLC in H$_2$O and D$_2$O, respectively. (3) Trial 2 had a very low polarization, making it impossible to calculate T_1. (4) pH* is a direct reading in a D$_2$O solution of the H$_2$O-calibrated pH meter.[38]

spectrometer and acquired dynamic spectra with a 4.5 s temporal resolution and 5° flip angle RF excitation pulse. Following the fourth−sixth acquisition steps, we added 3 equiv of NaOH solution through capillary tubing. The HP ^{13}C-GLC signal (158.6 ppm) disappeared immediately with the concomitant appearance of two very close resonances at (160.5 and 160.2 ppm, Figure 2c,d), implying a very fast and simultaneous ring-opening hydrolysis procedure from each side of ^{13}C-GLC to form two linear intermediates, as proposed in Figure 2f. The second hydrolysis step involving the breakdown of the intermediates to HP ^{13}CO$_3^{2-}$ (169.5 ppm) was the rate-determining step, suggesting that the elimination of the dipole−dipole interactions by replacing H$_2$O with D$_2$O increases the polarization. This hypothesis is supported by a doubling of T_1 values of the reaction intermediates and a tripling of T_1 of HP ^{13}CO$_3^{2-}$ produced in D$_2$O compared to that in H$_2$O (Table 2).

Table 2. List of Apparent T_1 (s) of All of the Components[a]

experiment conditions	interm I	interm II	^{13}CO$_3^{2-}$	H^{13}CO$_3^-$	^{13}CO$_2$
HP ^{13}C-GLC + 3 equiv NaOH in H$_2$O (Figure 2c)	21.9	18.5	54.0		
HP ^{13}C-GLC + 3 equiv NaOH in D$_2$O (Figure 2d)	43.2	38.5	155.3		
HP ^{13}C-GLC + 2 equiv of NaOH + Neut. Med. in D$_2$O (Figure 2e)	26.8	16.6	~103*	23.6	24.8

[a](1) Interm = intermediate; Neut. Med. = neutralization media. (2) The experiment was conducted at room temperature. (3) *In this time frame, most of the data points recorded the formation of ^{13}CO$_3^{2-}$ with a tendency of increasing intensity, while only the last few of time points were used to calculate T_1.

We attempted to minimize the usage of NaOH for a rapid ^{13}C-GLC breakdown in Trials 6 and 7 (Table 1) and utilized 2.0 equiv of NaOH to react with ^{13}C-GLC (Trial 6) in the subsequent formulation studies.

Investigation of HP ^{13}CO$_3^{2-}$ Solution Neutralization and Processing Procedure. Next, we neutralized the solution with an acid to convert HP ^{13}CO$_3^{2-}$ to HP H^{13}CO$_3^-$ at a physiological pH for human injection (Table 3). We observed

Table 3. Optimization of Neutralization Conditions to Prepare HP $H^{13}CO_3^-$ Formula in D_2O

trial no.	neut. med.	molar ratio of Tris/GLC	time after dissolution (s)	T_1 at 1.4 T (s)	%Pol of the first spectrum	pH*[38]
8	DCl (1 M)		62		<1.0	8.54
9	Citric acid (5 M)		67	63.8	16.4	7.39
10	Tris·HCl (1.0 M)/DCl (1.0 M)	1.40	64	59.7	15.6	7.30
11	Tris(1.2 M)/DCl(2.0 M)	2.25	57		3.2	7.30
12	Tris(1.2 M)/DCl(1.5 M)	2.40	61	59.5	16.3	7.78
13 (n = 7)	Tris(1.5 M)/DCl(1.5 M)	3.00	51 ± 2	66 ± 8	44 ± 2	7.76 ± 0.05

that a strong acid, such as deuterium chloride (DCl), compromised $H^{13}CO_3^-$ polarization (Trial 8). In contrast, a weak acid (citric acid) produced a much higher polarization of 16.4% at 67 s after dissolution with a long T_1 of 63.8 s (Trial 9). We hypothesized that a buffer system created by a weak acid might prevent the abrupt formation and escape of CO_2. We tested this hypothesis using a mixture of 1.0 M tris-(hydroxymethyl)aminomethane hydrochloride (Tris·HCl) and 1.0 M DCl in D_2O and found that it produced a similar polarization (15.6% at 64 s after dissolution, Trial 10) to Trial 9. Concerned with the potential toxicity of an intravenous injection of citric acid[39] and a lack of availability of pharmaceutical grade of Tris·HCl, we decided to use a mixture of Tris and DCl and found increasing Tris while decreasing DCl concentration could retain a higher polarization (Trials 11−13).

After carefully investigating the correlation between polarization level, solution osmolality, and probe concentration, we determined that the optimal neutralization media was a 1:1 mixture of Tris and DCl (1.5 M) in D_2O with a close to neutral pH* ∼ 6.7. Adding this medium to a molar ratio of Tris/^{13}C-GLC = 3 resulted in neutralizing the HP probe formulation to a pH* of 7.76 ± 0.05 with a dilution factor of 40%. Furthermore, we passed the neutralized solution through a preactivated C18 cartridge and then a 0.2 μm sterile filter to remove the trityl radical and generate a sterilized solution (Figure S4). The mean polarization level of HP $H^{13}CO_3^-$ obtained at 51 ± 2 s after dissolution was 44 ± 2% with a T_1 of 66 ± 8 s at 1.4 T (n = 7, Table S1, Trial 13).

We used dynamic HP ^{13}C NMR again to investigate the optimized HP $H^{13}CO_3^-$ formulation procedure (Figure 2e). After adding 2 equiv of NaOH, we waited for ∼60 s to allow for an almost complete breakdown of ^{13}C-GLC before neutralizing it. Similar results were observed compared to the addition of 3 equiv of NaOH in D_2O but with shorter T_1 values for the hydrolytic products (Table 2). Following neutralization with Tris/DCl, the conversion of HP $^{13}CO_3^{2-}$ (169.7 ppm) to HP $H^{13}CO_3^-$ (161.6 ppm) and then to HP $^{13}CO_2$ (125.5 ppm) was observed in the HP ^{13}C NMR spectra (Figure 2e). Trace amounts of intermediate signals arising from the ring-opening hydrolysis of each side of HP ^{13}C-GLC stayed at 160.1 and 159.7 ppm. Three new small signals appeared after adding neutralization media are assignable adducts of Tris−$^{13}CO_3^{2-}$ (165.0 ppm), glycerol−$H^{13}CO_3^-$ (159.3 ppm), and Tris−$^{13}CO_3^{2-}$ (158.6 ppm) labeled as Adducts I−III in Figure 2e-ii, respectively.[21,40] We confirmed the identity of each adduct by mixing $H^{13}CO_3^-$, glycerol, and Tris and evaluated their pH sensitivity and stability (Figures S6−S10). We demonstrated the adducts disappeared upon dilution, suggesting that they are unstable and only observable at equilibrium in the presence of high concentrations of the above mixtures (Figures S9, S10). These results demonstrated that the adducts would unlikely persist *in vivo* as a toxicity concern.

Overall, these results identified the key factors for producing an HP $H^{13}CO_3^-$ formulation suitable for clinical use, including using D_2O as the dissolution media rather than H_2O and a weak acid−base buffer system for neutralization following saponification of the precursor HP ^{13}C-GLC.

Development of a Postdissolution Processing Apparatus for Producing the HP $H^{13}CO_3^-$ Formula. Due to the novelty and complexity of the conversion of the precursor, HP ^{13}C-GLC, to injectable HP $H^{13}CO_3^-$, there are no commercially available postdissolution processing and QC systems, such as those integrated into the SPINlab polarizer for the clinical HP ^{13}C-pyruvate studies. We designed an apparatus consisting of hydrolysis, neutralization, trityl radical removal, and sterile filtration units to prepare HP $H^{13}CO_3^-$ along with mechanisms for QC testing (Figure 3).

A brief procedure is as follows: ^{13}C-GLC/trityl radical (793 mg) is added to a cryovial ① and polarized at 0.8 K for 4.5 h. A dissolution syringe ② filled with pressurized and superheated D_2O (38 mL) is used to dissolve the probe and transfer it into a receiver vessel ③ filled with 4 M NaOH (3.28 mL). After 10 s, the stopcock valve ④ is opened to allow the solution to flow into a two-necked, round-bottomed flask ⑤ containing 13.1 mL of neutralization media (1.5 M equivalent mixture of Tris/DCl in D_2O) cooled to −18 °C in an ice/salt bath. The mixing is kept under stirring by using a stir bar on a stir plate. By closing valve ④ and opening the N_2 gas inlet ⑥ and three-way stopcock ⑧, the solution is pushed through four C18 cartridges installed in parallel between two manifolds ⑦ to remove the trityl radical. At last, the solution passes through a 0.2 μm terminal sterilization filter ⑧ into a MedRad syringe ⑨ for patient administration with an aliquot saved for QC testing. As the commonly used mechanical filter, which relies on its pores to capture the trityl radical particles precipitated at a low pH (∼4) by HP ^{13}C-pyruvic acid, is not suitable for our study, we selected reserve-phase C18 cartridges to capture the nonpolar trityl radicals, while allowing polar HP $H^{13}CO_3^-$ to elute through easily. The efficiency of this method is demonstrated in Figure S11, where the residual concentration of trityl radicals is undetectable by a UV/vis spectrometer integrated into the GE MPQC system used for the quality control of HP ^{13}C-pyruvate clinical studies. The postdissolution processing procedure can be completed in approximately 50 s, which is comparable to the time required by the GE automatic fluid handler with HP ^{13}C-pyruvate injection. Moreover, the procedure is performed in the vicinity of 3T and 7T GE clinical MRI scanners and the 5T GE Spinlab polarizer, thereby ensuring that the polarization level is preserved by avoiding the zero-field effect.[41]

Hyperpolarized and thermal equilibrium ^{13}C NMR spectra (Figure 3b,c) showed identical resonances: the dominant peaks of $H^{13}CO_3^-$ (161.4 ppm) and $^{13}CO_2$ (125.5 ppm), three minor peaks of semistable adducts, Tris−$^{13}CO_3^{2-}$ (165.0 ppm), glycerol−$H^{13}CO_3^-$ (160.2 ppm), and Tris−$H^{13}CO_3^-$ (159.9 ppm) labeled as Adducts I−III, respectively, except $^{13}CO_3^{2-}$
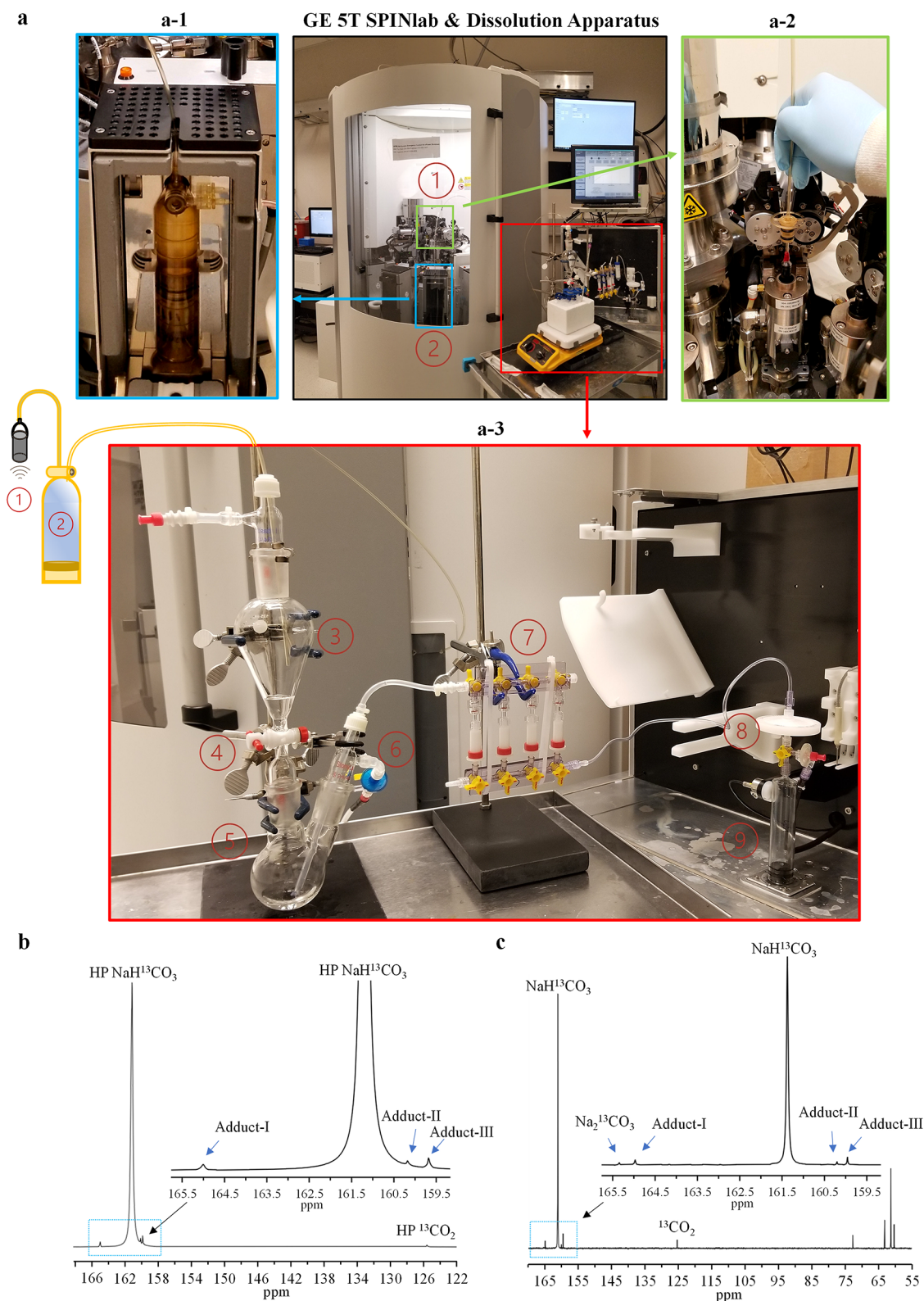
Figure 3. Apparatus and process for preparing HP $H^{13}CO_3^-$ for clinical studies. (a) GE 5T SPINlab polarizer, (a-1) loading dissolution syringe into a heater console, (a-2) loading a cryovial filled with a probe for polarization, and (a-3) customized postdissolution reaction and processing system. (b) First observed HP ^{13}C NMR spectrum on the Pulsar NMR spectrometer (1.4 T). (c) Averaged thermal equilibrium ^{13}C NMR spectrum (400 scans) acquired on a 9.4 T ^{13}C NMR spectrometer showing the identical signals arising in the hyperpolarized state.

(165.4 ppm) and signals from natural abundance of ^{13}C in glycerol (72.9 and 63.3 ppm) and tris (62.2 and 59.6 ppm) in the thermal state (Figure 3c). Percent polarization of $H^{13}CO_3^-$ was 20.1% at 57 s, T_1 = 65.8 s at 1.4 T. There was a notable absence

of the intermediate species identified in Figure 2e-ii, possibly because the elevated temperature (75 °C) in the dissolution led to a complete breakdown of HP ^{13}C-GLC compared to room temperature in the NMR spectrometer.
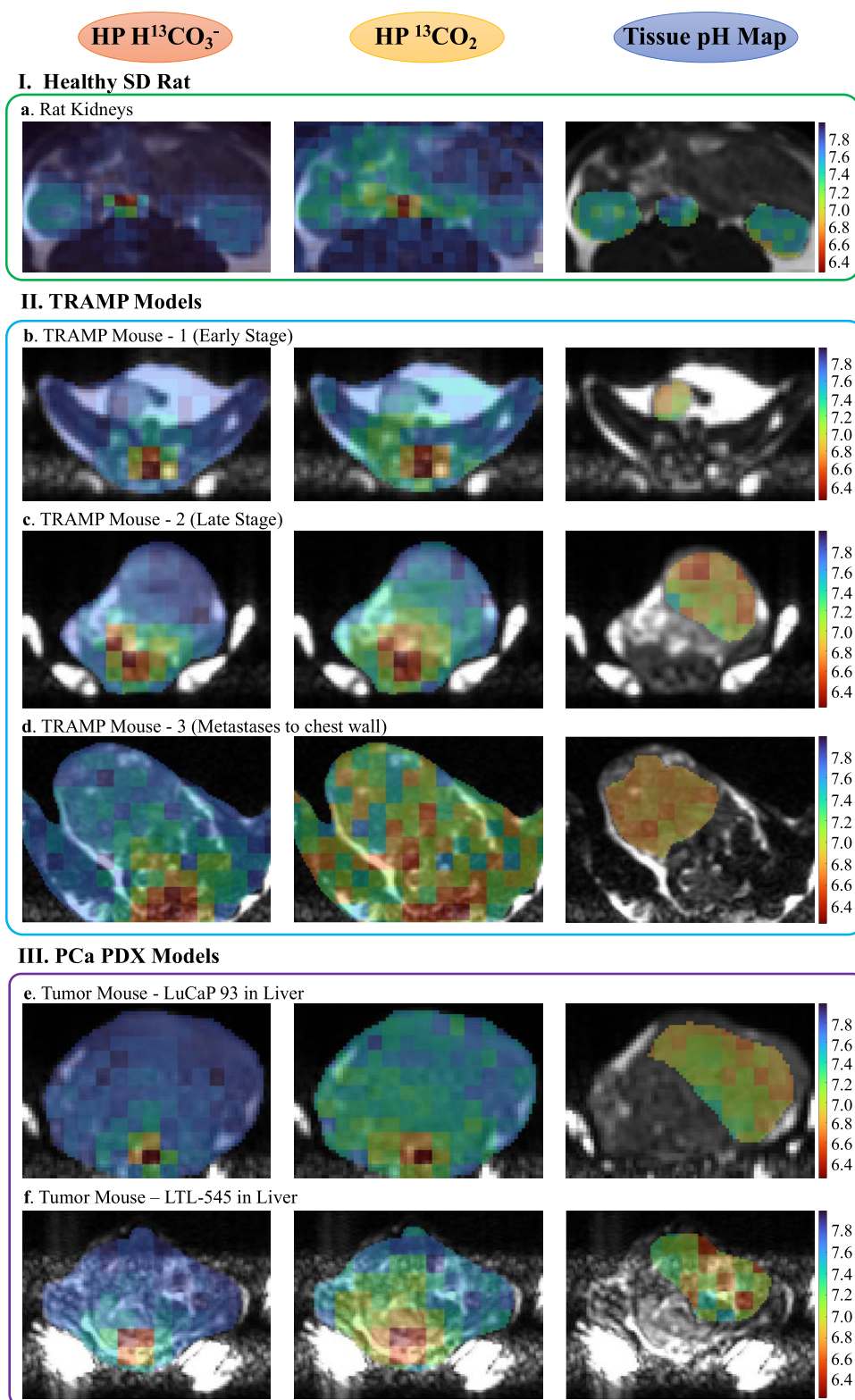
Figure 4. HP ^{13}C MRI pH$_e$ imaging studies in animal models. The figures on the left, middle, and right columns show the ^{13}C MRI images of HP H^{13}CO$_3^-$, HP ^{13}CO$_2$, and pH$_e$ maps overlaid with anatomical proton MRI figures, respectively. pH$_e$ maps are shown in the regions of interest.

Toxicology Studies. We injected the HP H^{13}CO$_3^-$ solution into a cohort of three adult Sprague−Dawley (SD) rats for toxicology studies, as detailed in the Experimental Section. All of the injections were well tolerated without any observed acute pathological changes or abnormalities of major organs (Tables S2−S5). These data support the potential suitability of the HP H^{13}CO$_3^-$ formulation for use in humans.

In Vivo HP ^{13}C MRI pH$_e$ Imaging Studies. We evaluated this method with various *in vivo* models, including healthy adult SD rats, TRAMP mice at different stages and with
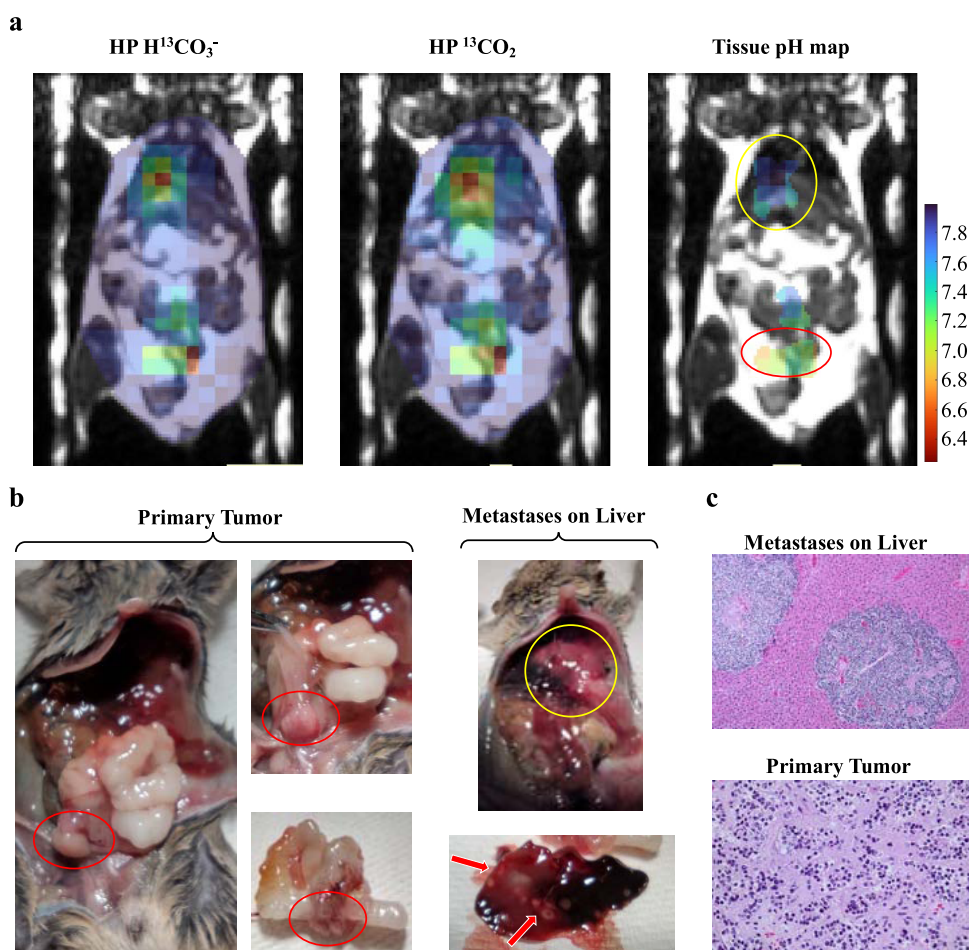
Figure 5. HP ^{13}C MRI pH$_e$ imaging studies with TRAMP prostate cancer mouse, which has metastases on the liver. (a) ^{13}C MRI images of HP H^{13}CO$_3^-$, HP ^{13}CO$_2$, and pH map; the red circle is the primary tumor, and the yellow circle is the metastases on the liver. (b) Dissection of the mouse to show the primary tumor and metastases. (c) Histological studies showing the tissue segments of primary tumor and metastases.

metastases,[42,43] and patient-derived xenograft (PDX, LuCaP 93, and LTL-545 PCa) mouse models implanted in the liver.[44,45]

We found that the SD rat kidneys have heterogeneous pH 7.47 ± 0.06 in the cortex and pH 7.28 ± 0.10 in the medullary region (Figure 4a). The results were similar to the pH meter measurements of 7.07 ± 0.06 and 6.92 ± 0.06, respectively, from shallow and central positions at three different locations, as well as literature reports using different methods for the renal cortex (pH 7.0−7.3), the medulla (pH 6.8−7. 0), and the calyx-ureter (pH 6.3−6.5).[46−50]

In total, we imaged four TRAMP mice, including two with metastases. For the mice with localized tumors, we compared two with a large difference in tumor volume: 0.5 and 2 cm^3, which corresponded to pH 6.90 ± 0.10 and pH 6.86 ± 0.09, respectively (Figure 4b,c). The pH electrode measurement of the large-volume tumor was pH 6.86 ± 0.05 at three locations. The third had metastases and developed a 2 cm^3 solid tumor on the chest wall (Figure 4d). The imaged pH of the metastasis (pH 6.67 ± 0.07) agreed with the microelectrode value of pH 6.72 ± 0.05, which is more acidic than the primary tumor at pH ∼ 6.8 (Figure 4c). Similarly, both LuCaP 93 and LTL-545 PDX liver tumors had low pH$_e$ values of 6.99 ± 0.09 and 6.84 ± 0.09, which agreed well with the electrode measurements of pH$_e$ 6.91 ± 0.14 and 7.01 ± 0.18 at three tumor locations, respectively (Figure 4e,f). This suggests a correlation between the low pH$_e$ and the

high-grade and aggressive stages of PCa, as previously reported.[22]

We imaged a fourth TRAMP mouse in the coronal plane for detecting the spread of metastases (Figure 5a). Interestingly, both primary tumor and liver metastases exhibited elevated signals of HP H^{13}CO$_3^-$ and HP ^{13}CO$_2$, potentially due to the high vascular permeability in cancers.[51] The tumors were identified by the dissection and histology studies (Figure 5b,c). The imaged pH$_e$ of the primary tumor was 6.94 ± 0.06, which agreed well with the electrode-measured pH 6.90 ± 0.02. However, the imaged pH$_e$ on the liver metastasis (pH ∼ 7.4) was higher than the electrode-measured value (pH 6.64 ± 0.06), possibly due to the respiratory motion artifact causing partial volume averaging. T$_2$-weighted ^{1}H MRI of anatomic images are presented in Figure S12.

To validate the reliability of our pH imaging method, we performed a phantom study using two phosphate buffer solutions prepared at tumoral pH 6.60 and healthy physiological pH 7.40 in the presence of carbonic anhydrase.[18] The imaged pH values were 6.67 ± 0.05 and 7.35 ± 0.05, similar to the pH values of 6.56 and 7.43 measured on the pH meter shortly after the experiment, demonstrating a satisfactory level of accuracy (Figure S13).

DISCUSSION

Changes in tumoral pH_e, which result from alterations in tumor intrinsic metabolism and the TME, are attractive biomarkers for studying tumor biology, disease progression, and response to therapy. Thus, there has been extensive interest in developing noninvasive imaging methods for measuring pH_e in laboratory and clinical settings. In this study, we developed a patient-ready method to produce a highly concentrated and polarized $H^{13}CO_3^-$ solution and applied it to a series of clinically relevant prostate cancer models. These methods will be directly employed in future clinical studies of PCa patients.

Instead of directly polarizing $H^{13}CO_3^-$, which suffers from low polarization, low concentrations, and high toxicity concerns,[18] we broke down a readily polarized nontoxic organic compound ^{13}C-GLC via a base-catalyzed hydrolysis followed by neutralization to produce highly polarized $H^{13}CO_3^-$.[21] One limitation of the current method is the long polarization time of 7 h, compared to 1.5 or 2 h for $NaH^{13}CO_3$ or $CsH^{13}CO_3$, respectively. We explored the mechanism of ^{13}C-GLC hydrolysis in the hyperpolarized state, and our finding experimentally verified the previously proposed two-step ring-opening procedure[52] and revealed the second hydrolysis reaction as the rate-limiting step (Figure 2f). The mechanistic HP studies also supported our decision to use D_2O for dissolution, which diminishes dipole−dipole relaxation and preserves polarization. It is also worth mentioning that D_2O is safe for human injection, consistent with our toxicology studies.[53,54] Furthermore, we identified a buffer system that can ensure physiological pH for injection and reduce polarization loss from the rapid formation of escaping CO_2. When compared against the other methods previously reported for the preparation of hyperpolarized $H^{13}CO_3^-$, our method has the advantages of higher polarization, higher concentration, and the lack of using potentially toxic components (Tables S6 and S7). This accomplishment made further studies possible and represents a significant milestone toward clinical application.

The intrinsically low concentration of HP $^{13}CO_2$ at physiologic pH and high perfusion *in vivo* pose a challenge for imaging acquisition. Thus, we designed a spiral-GRE sequence with flow suppression.[27,33] Due to the short echo time, this sequence exhibits advantages in improving the SNR, which is particularly helpful for detecting HP $^{13}CO_2$, ensuring higher spatial resolution and improved image quality compared to data previously acquired using 2D-EPI and 2D-CSI sequences.[22,55] Furthermore, the flow suppression gradients eliminated a strong signal arising from HP $H^{13}CO_3^-$ in the arteries along the animal head-to-tail direction, reducing artifacts of both HP $H^{13}CO_3^-$ and HP $^{13}CO_2$ images and further improving the accuracy of pH_e imaging.[33]

We validated the clinical application feasibility of this imaging method in healthy rats and tumor-bearing mouse models. We first evaluated the accuracy by imaging the pH gradient between the cortex and the medullary regions in rat kidneys. We also imaged TRAMP mice with low-grade and high-grade tumors, which recapitulates the features of human PCa progression.[43] The results were consistent with our prior studies, showing that gradual acidification in tumors occurs during tumor progression.[22] Moreover, we demonstrated that metastases have much lower extracellular pH values compared to those of the primary tumors. Next, we imaged two types of high-grade PDX models with neuroendocrine prostate cancer features, LuCaP 93[56] and LTL-545,[44] revealing tumoral acidification as

previously found in high-grade TRAMP tumors. The lower pH_e found in TRAMP metastases as well as these aggressive PDX models supports our hypothesis that tumoral acidification may represent a biomarker for the presence of aggressive and potentially lethal PCa.

TRANSLATIONAL OUTLOOK

Beyond theoretical studies and *in vivo* validation, we developed SOPs for routinely preparing an HP $H^{13}CO_3^-$ formulation using a clinical polarizer and our purpose-built apparatus. Following GMP guidelines in the U.S. Code of Federal Regulation Title 21, Part 212, we can produce a highly polarized $H^{13}CO_3^-$ formulation within 50 s with major components at approximate concentrations: $H^{13}CO_3^-$ (120 mM), glycerol (130 mM), Tris buffer (380 mM), and NaCl (255 mM) in 35 mL of D_2O. The QC testing confirms that the $H^{13}CO_3^-$ formulation is radical-free and sterile, has near physiologic pH (∼7.8), and has a suitable volume (∼35 mL) for human injection. Tris is considered safe for human injection, even at relatively high concentrations compared to other buffer materials. For instance, routine HP ^{13}C-pyruvate studies involve an injection of 100 mM Tris,[27] and Tham solution, used to prevent and correct metabolic acidosis, is injected at a concentration of 300 mM.[57] Assuming an average human adult blood volume of 6 L, the final concentrations of major buffer materials $H^{13}CO_3^-$ and Tris are diluted to ∼0.6 and ∼2.2 mM, respectively, which have minimal impact on the original tissue pH compared to the endogenous concentration of bicarbonate (22−32 mM) in blood. These data were used to obtain approval from the FDA (IND# 165528) and IRB for our study to proceed with the clinical trials using this pH_e imaging method in PCa patients (NCT05851365).

Overall, tissue acidosis, a hallmark of various diseases, has prompted extensive efforts to develop noninvasive imaging methods, as we and others have previously reviewed.[8,9,13,19] Spectroscopic probes for MRS, such as ^{31}P and ^{19}F, lack sensitivity and have small pH-dependent chemical shifts.[58,59] Other ^1H MRI techniques, like CEST or using Gd^{3+}, face difficulties in accurately determining probe concentrations *in vivo*.[60−63] Some probes measure only intracellular pH, limiting their responsiveness to metabolic changes in the extracellular space. In this work, we have developed a new methodology to produce highly polarized, high-concentration, large-volume, sterilized, safe, and human-injectable $H^{13}CO_3^-$. This advancement enables high-resolution MRI imaging acquisition, overcoming previous limitations and enhancing the potential for clinical translation of pH mapping techniques.[18]

CONCLUSIONS

In this study, we developed a patient-ready method to produce a highly concentrated and polarized $H^{13}CO_3^-$ solution and applied it to a series of clinically relevant prostate cancer models. To overcome unexpected difficulties in the loss of polarization during preparation, we conducted mechanistic studies to determine the reaction course. These insights were used to develop an optimized processing method and a customized reaction apparatus that can routinely produce an HP $H^{13}CO_3^-$ contrast agent for patient injection. Using an optimized pulse sequence, we validated these methods in imaging healthy and prostate cancer preclinical models, demonstrating acidification in healthy kidney and prostate tumor tissue. These methods will be employed for subsequent clinical studies.

■ ASSOCIATED CONTENT

Ⓢ Supporting Information

The Supporting Information is available free of charge at https://pubs.acs.org/doi/10.1021/acssensors.3c00851.

NMR data acquisition parameters; investigation of the GLC hydrolysis mechanism by NMR in the thermal equilibrium state; condition optimization for producing the HP $H^{13}CO_3^-$ formula in one-fourth of clinical dose; investigation of the adduct formation, pH sensitivity, and stability; characterization of the residual concentration of AH111501 in final HP $H^{13}CO_3^-$ injection; toxicology studies with Sprague—Dawley rats; comparison of methods of producing polarized $H^{13}CO_3^-$; T_2-weighted proton MRI images of animal models; and validation of the hyperpolarized ^{13}C MRI pH_e imaging method in phantoms (PDF)

■ AUTHOR INFORMATION

Corresponding Author

Robert R. Flavell — *Department of Radiology and Biomedical Imaging, University of California, San Francisco, San Francisco, California 94107, United States; Department of Pharmaceutical Chemistry, University of California, San Francisco, California 94158, United States;* ⓞ orcid.org/0000-0002-8694-1199; Email: Robert.flavell@ucsf.edu

Authors

Changhua Mu — *Department of Radiology and Biomedical Imaging, University of California, San Francisco, San Francisco, California 94107, United States;* ⓞ orcid.org/0000-0002-5007-0133

Xiaoxi Liu — *Department of Radiology and Biomedical Imaging, University of California, San Francisco, San Francisco, California 94107, United States*

Yaewon Kim — *Department of Radiology and Biomedical Imaging, University of California, San Francisco, San Francisco, California 94107, United States*

Andrew Riselli — *Department of Radiology and Biomedical Imaging, University of California, San Francisco, San Francisco, California 94107, United States*

David E. Korenchan — *Department of Radiology and Biomedical Imaging, University of California, San Francisco, San Francisco, California 94107, United States; Present Address: Department of Radiology, Athinoula A. Martinos Center for Biomedical Imaging, Massachusetts General Hospital and Harvard Medical School, Charlestown, Massachusetts 02114, United States;* ⓞ orcid.org/0000-0001-6152-5896

Robert A. Bok — *Department of Radiology and Biomedical Imaging, University of California, San Francisco, San Francisco, California 94107, United States*

Romelyn Delos Santos — *Department of Radiology and Biomedical Imaging, University of California, San Francisco, San Francisco, California 94107, United States*

Renuka Sriram — *Department of Radiology and Biomedical Imaging, University of California, San Francisco, San Francisco, California 94107, United States;* ⓞ orcid.org/0000-0003-3505-2479

Hecong Qin — *Department of Radiology and Biomedical Imaging, University of California, San Francisco, San Francisco, California 94107, United States; Present*

Address: Pritzker School of Medicine, The University of Chicago, Chicago, Illinois 60637, United State.

Hao Nguyen — *Department of Urology, University of California, San Francisco, California 94143, United States*

Jeremy W. Gordon — *Department of Radiology and Biomedical Imaging, University of California, San Francisco, San Francisco, California 94107, United States;* ⓞ orcid.org/0000-0003-2760-4886

James Slater — *Department of Radiology and Biomedical Imaging, University of California, San Francisco, San Francisco, California 94107, United States*

Peder E. Z. Larson — *Department of Radiology and Biomedical Imaging, University of California, San Francisco, San Francisco, California 94107, United States*

Daniel B. Vigneron — *Department of Radiology and Biomedical Imaging, University of California, San Francisco, San Francisco, California 94107, United States*

John Kurhanewicz — *Department of Radiology and Biomedical Imaging, University of California, San Francisco, San Francisco, California 94107, United States*

David M. Wilson — *Department of Radiology and Biomedical Imaging, University of California, San Francisco, San Francisco, California 94107, United States;* ⓞ orcid.org/0000-0002-1095-046X

Complete contact information is available at:
https://pubs.acs.org/10.1021/acssensors.3c00851

Author Contributions

C.M. designed, performed, and participated in all of the experiments; analyzed the data; created protocols and the SOPs; prepared the IND application documents; and wrote the manuscript. X.L. designed the pulse sequence, conducted the animal imaging experiment and data analysis, provided *in vivo* imaging data, and wrote the imaging section. Y.K., A.R., and D.E.K. participated in experiments. R.A.B. performed animal handling, toxicity tests, and analyses; provided dissection figures; and conducted data analysis. R.S. prepared PDX tumor mice. R.D.S. assisted in animal handling for toxicity tests, performed histology studies, and provided histology data. H.Q., H.N., J.W.G., J.S., P.E.Z.L, D.V., J.K., and D.M.W. provided knowledges for the project. R.R.F. conceived the study, supervised and supported the entire research project, directed the experiments, and wrote and edited the manuscripts. All authors read, discussed, edited, and revised the manuscript.

Notes

The authors declare no competing financial interest.

■ ACKNOWLEDGMENTS

■ REFERENCES

(1) Siegel, R. L.; Miller, K. D.; Wagle, N. S.; Jemal, A. Cancer Statistics, 2023. *Ca-Cancer J. Clin.* **2023**, 72, 17−48.

(2) Klein, E. A. Prostate cancer: Risk stratification and choice ofinitial treatment https://www.uptodate.com/contents/localized-prostate-cancer-risk-stratification-and-choice-of-initial-treatment (accessed Apr 3, 2022).

(3) Picchio, M.; Mapelli, P.; Panebianco, V.; Castellucci, P.; Incerti, E.; Briganti, A.; Gandaglia, G.; Kirienko, M.; Barchetti, F.; Nanni, C.; et al. Imaging Biomarkers in Prostate Cancer: Role of PET/CT and MRI. *Eur. J. Nucl. Med. Mol. Imaging* **2015**, *42*, 644−655.

(4) Couñago, F.; López-Campos, F.; Díaz-Gavela, A. A.; Almagro, E.; Fenández-Pascual, E.; Henríquez, I.; Lozano, R.; Linares Espinós, E.; Gómez-Iturriaga, A.; de Velasco, G.; et al. Clinical Applications of Molecular Biomarkers in Prostate Cancer. *Cancers* **2020**, *12*, No. 1550.

(5) Duffy, M. J. Biomarkers for Prostate Cancer: Prostate-Specific Antigen and Beyond. *Clin. Chem. Lab. Med.* **2020**, *58*, 326−339.

(6) Saini, S. PSA and beyond: Alternative Prostate Cancer Biomarkers. *Cell Oncol.* **2016**, *39*, 97−106.

(7) Warburg, O. On the Origin of Cancer Cells. *Science* **1956**, *123*, 309−314.

(8) Mu, C.; Korenchan, D. E.; Wang, S.; Wilson, D. M.; Flavell, R. R. Tumor Microenvironment Biosensors for Hyperpolarized Carbon-13 Magnetic Resonance Spectroscopy. *Mol. Imaging Biol.* **2021**, *23*, 323−334.

(9) Gillies, R. J.; Raghunand, N.; Garcia-Martin, M. L.; Gatenby, R. A. PH Imaging. A Review of PH Measurement Methods and Applications in Cancers. *IEEE Eng. Med. Biol. Mag.* **2004**, *23*, 57−64.

(10) Gatenby, R. A.; Gawlinski, E. T.; Gmitro, A. F.; Kaylor, B.; Gillies, R. J. Acid-Mediated Tumor Invasion: A Multidisciplinary Study. *Cancer Res.* **2006**, *66*, 5216−5223.

(11) Kato, Y.; Ozawa, S.; Miyamoto, C.; Maehata, Y.; Suzuki, A.; Maeda, T.; Baba, Y. Acidic Extracellular Microenvironment and Cancer. *Cancer Cell Int.* **2013**, *13*, 89.

(12) Webb, B. A.; Chimenti, M.; Jacobson, M. P.; Barber, D. L. Dysregulated PH: A Perfect Storm for Cancer Progression. *Nat. Rev. Cancer* **2011**, *11*, 671−677.

(13) Korenchan, D. E.; Flavell, R. R. Spatiotemporal Ph Heterogeneity as a Promoter of Cancer Progression and Therapeutic Resistance. *Cancers* **2019**, *11*, No. 1026. DOI: 10.3390/cancers11071026.

(14) Neri, D.; Supuran, C. T. Interfering with PH Regulation in Tumours as a Therapeutic Strategy. *Nat. Rev. Drug Discovery* **2011**, *10*, 767−777.

(15) Anemone, A.; Consolino, L.; Arena, F.; Capozza, M.; Longo, D. L. Imaging Tumor Acidosis: A Survey of the Available Techniques for Mapping in Vivo Tumor PH. *Cancer Metastasis Rev.* **2019**, *38*, 25−49.

(16) Stubbs, M.; Bhujwalla, Z. M.; Tozer, G. M.; Rodrigues, L. M.; Maxwell, R. J.; Morgan, R.; Howe, F. A.; Griffiths, J. R. An Assessment Of 31P MRS as a Method of Measuring PH in Rat Tumours. *NMR Biomed.* **1992**, *5*, 351−359.

(17) Shimolina, L.; Potekhina, E.; Druzhkova, I.; Lukina, M.; Dudenkova, V.; Belousov, V.; Shcheslavskiy, V.; Zagaynova, E.; Shirmanova, M. Fluorescence Lifetime-Based PH Mapping of Tumors in Vivo Using Genetically Encoded Sensor SypHerRed. *Biophys. J.* **2022**, *121*, 1156−1165.

(18) Gallagher, F. A.; Kettunen, M. I.; Day, S. E.; Hu, D.-E.; Ardenkjær-Larsen, J. H.; Zandt, R. in ′t.; Jensen, P. R.; Karlsson, M.; Golman, K.; Lerche, M. H. Magnetic Resonance Imaging of PH in Vivo Using Hyperpolarized 13C-Labelled Bicarbonate. *Nature* **2008**, *453*, 940−943.

(19) Gallagher, F. A.; Kettunen, M. I.; Brindle, K. M. Imaging PH with Hyperpolarized 13C. *NMR Biomed.* **2011**, *24*, 1006−1015.

(20) Ghosh, R. K.; Kadlecek, S. J.; Pourfathi, M.; Rizi, R. R. Efficient Production of Hyperpolarized Bicarbonate by Chemical Reaction on a DNP Precursor to Measure PH. *Magn. Reson. Med.* **2015**, *74*, 1406−1413.

(21) Korenchan, D. E.; Flavell, R. R.; Baligand, C.; Sriram, R.; Neumann, K.; Sukumar, S.; VanBrocklin, H.; Vigneron, D. B.; Wilson, D. M.; Kurhanewicz, J. Dynamic Nuclear Polarization of Biocompatible (13)C-Enriched Carbonates for in Vivo PH Imaging. *Chem. Commun.* **2016**, *52*, 3030−3033.

(22) Korenchan, D. E.; Bok, R.; Sriram, R.; Liu, K.; Santos, R. D.; Qin, H.; Lobach, I.; Korn, N.; Wilson, D. M.; Kurhanewicz, J.; Flavell, R. R. Hyperpolarized in Vivo PH Imaging Reveals Grade-Dependent Acidification in Prostate Cancer. *Oncotarget* **2019**, *10*, 6096−6110.

(23) Flavell, R. R.; von Morze, C.; Blecha, J. E.; Korenchan, D. E.; Van Criekinge, M.; Sriram, R.; Gordon, J. W.; Chen, H.-Y.; Subramaniam, S.; Bok, R. A.; et al. Application of Good's Buffers to PH Imaging Using Hyperpolarized (13)C MRI. *Chem. Commun.* **2015**, *51*, 14119−14122.

(24) Hundshammer, C.; Düwel, S.; Schilling, F. Imaging of Extracellular Ph Using Hyperpolarized Molecules. *Isr. J. Chem.* **2017**, *57*, 788−799.

(25) Nelson, S. J.; Kurhanewicz, J.; Vigneron, D. B.; Larson, P. E. Z.; Harzstark, A. L.; Ferrone, M.; van Criekinge, M.; Chang, J. W.; Bok, R.; Park, I.; et al. Metabolic Imaging of Patients with Prostate Cancer Using Hyperpolarized [1-^{13}C]Pyruvate. *Sci. Transl. Med.* **2013**, *5*, No. 198ra108.

(26) Qin, H.; Tang, S.; Riselli, A. M.; Bok, R. A.; Delos Santos, R.; van Criekinge, M.; Gordon, J. W.; Aggarwal, R.; Chen, R.; Goddard, G.; et al. Clinical Translation of Hyperpolarized 13 C Pyruvate and Urea MRI for Simultaneous Metabolic and Perfusion Imaging. *Magn. Reson. Med.* **2022**, *87*, 138−149.

(27) Liu, X.; Tang, S.; Mu, C.; Qin, H.; Cui, D.; Lai, Y.-C.; Riselli, A. M.; Delos Santos, R.; Carvajal, L.; Gebrezgiabhier, D.; et al. Development of Specialized Magnetic Resonance Acquisition Techniques for Human Hyperpolarized [13 C,15 N2]Urea + [1−13 C]Pyruvate Simultaneous Perfusion and Metabolic Imaging. *Magn. Reson. Med.* **2022**, *88*, 1039−1054.

(28) Willcott, M. R. MestRe Nova MestRe Nova. Mestrelab Research S.L. Feliciano Barrera 9B, Bajo, 15706 Santiago de Compostela, Spain. Http://Www.Mestrelab.Com. *J. Am. Chem. Soc.* **2009**, *131*, 13180−13180.

(29) Mestrelab Research S.L. *MestReNova*; Mestrelab Research S.L., 2021.

(30) Tang, S.; Milshteyn, E.; Reed, G.; Gordon, J.; Bok, R.; Zhu, X.; Zhu, Z.; Vigneron, D. B.; Larson, P. E. Z. A Regional Bolus Tracking and Real-Time B1 Calibration Method for Hyperpolarized 13 C MRI. *Magn. Reson. Med.* **2019**, *81*, 839−851.

(31) Tang, S.; Bok, R.; Qin, H.; Reed, G.; VanCriekinge, M.; Delos Santos, R.; Overall, W.; Santos, J.; Gordon, J.; Wang, Z. J.; et al. A Metabolite-Specific 3D Stack-of-Spiral BSSFP Sequence for Improved Lactate Imaging in Hyperpolarized [1−13 C]Pyruvate Studies on a 3T Clinical Scanner. *Magn. Reson. Med.* **2020**, *84*, 1113−1125.

(32) Larson, P. E. Z.; Gordon, J. W. Hyperpolarized Metabolic MRI-Acquisition, Reconstruction, and Analysis Methods. *Metabolites* **2021**, *11*, No. 386. DOI: 10.3390/metabo11060386.

(33) Gordon, J. W.; Niles, D. J.; Adamson, E. B.; Johnson, K. M.; Fain, S. B. Application of Flow Sensitive Gradients for Improved Measures of Metabolism Using Hyperpolarized (13) c MRI. *Magn. Reson. Med.* **2016**, *75*, 1242−1248.

(34) Larson, P. Spectral-Spatial-RF-Pulse-Design https://github.com/LarsonLab/Spectral-Spatial-RF-Pulse-Design (accessed Apr 15, 2022).

(35) Kaur, A.; Prakash, R.; Ali, A. 1H NMR Assisted Quantification of Glycerol Carbonate in the Mixture of Glycerol and Glycerol Carbonate. *Talanta* **2018**, *178*, 1001−1005.

(36) Cheng, C.-Y.; Balsandorj, Z.; Hao, Z.; Pan, L. High-Precision Measurement of PH in the Full Toothpaste Using NMR Chemical Shift. *J. Magn. Reson.* **2020**, *317*, 106771.

(37) Cho, A.; Eskandari, R.; Miloushev, V. Z.; Keshari, K. R. A Non-Synthetic Approach to Extending the Lifetime of Hyperpolarized Molecules Using D2O Solvation. *J. Magn. Reson.* **2018**, *295*, 57−62.

(38) Mikkelsen, K.; Nielsen, S. O. Acidity Measurements with the Glass Electrode in H$_2$ O-D$_2$ O Mixtures. *J. Phys. Chem. A* **1960**, *64*, 632−637.

(39) Karlaganis, G. *SIDS Initial Assessment Report for 11th SIAM*; UNEP Publications, 2001, https://hpvchemicals.oecd.org/ui/handler.axd?id=ff78c453-36c1-430d-9034-63e15899d24b (accessed 2023-10-10).

(40) Park, J.-Y.; Yoon, S. J.; Lee, H. Effect of Steric Hindrance on Carbon Dioxide Absorption into New Amine Solutions: Thermodynamic and Spectroscopic Verification through Solubility and NMR Analysis. *Environ. Sci. Technol.* **2003**, *37*, 1670−1675.

(41) Kiryutin, A. S.; Rodin, B. A.; Yurkovskaya, A. V.; Ivanov, K. L.; Kurzbach, D.; Jannin, S.; Guarin, D.; Abergel, D.; Bodenhausen, G. Transport of Hyperpolarized Samples in Dissolution-DNP Experiments. *Phys. Chem. Chem. Phys.* **2019**, *21*, 13696−13705.

(42) Gingrich, J. R.; Greenberg, N. M. A Transgenic Mouse Prostate Cancer Model. *Toxicol. Pathol.* **1996**, *24*, 502−504.

(43) Gingrich, J. R.; Barrios, R. J.; Foster, B. A.; Greenberg, N. M. Pathologic Progression of Autochthonous Prostate Cancer in the TRAMP Model. *Prostate Cancer Prostatic Dis.* **1999**, *2*, 70−75.

(44) Lin, D.; Wyatt, A. W.; Xue, H.; Wang, Y.; Dong, X.; Haegert, A.; Wu, R.; Brahmbhatt, S.; Mo, F.; Jong, L.; et al. High Fidelity Patient-Derived Xenografts for Accelerating Prostate Cancer Discovery and Drug Development. *Cancer Res.* **2014**, *74*, 1272−1283.

(45) Sriram, R.; Gordon, J.; Baligand, C.; Ahamed, F.; Delos Santos, J.; Qin, H.; Bok, R. A.; Vigneron, D. B.; Kurhanewicz, J.; Larson, P. E. Z.; Wang, Z. Non-Invasive Assessment of Lactate Production and Compartmentalization in Renal Cell Carcinomas Using Hyperpolarized 13C Pyruvate MRI. *Cancers* **2018**, *10*, No. 313, DOI: 10.3390/cancers10090313.

(46) Wu, Y.; Zhou, I. Y.; Igarashi, T.; Longo, D. L.; Aime, S.; Sun, P. Z. A generalized ratiometric chemical exchange saturation transfer (CEST) MRI approach for mapping renal pH using iopamidol. *Magn. Reson. Med.* **2018**, *79*, 1553−1558.

(47) Raghunand, N.; Howison, C.; Sherry, A. D.; Zhang, S.; Gillies, R. J. Renal and systemic pH imaging by contrast-enhanced MRI. *Magn. Reson. Med.* **2003**, *49*, 249−257.

(48) Takahashi, S.; Kagami, Y.; Hanaoka, K.; Terai, T.; Komatsu, T.; Ueno, T.; Uchiyama, M.; Koyama-Honda, I.; Mizushima, N.; Taguchi, T.; Arai, H.; Nagano, T.; Urano, Y. Development of a series of practical fluorescent chemical tools to measure ph values in living samples. *J. Am. Chem. Soc.* **2018**, *140*, 5925−5933.

(49) Henderson, R. M.; Bell, P. B.; Cohen, R. D.; Browning, C.; Iles, R. A. Measurement of intracellular pH with microelectrodes in rat kidney in vivo. *Am. J. Physiol.* **1986**, *250*, F203−F209.

(50) Duwel, S.; Hundshammer, C.; Gersch, M.; Feuerecker, B.; Steiger, K.; Buck, A.; Walch, A.; Haase, A.; Glaser, S. J.; Schwaiger, M.; Schilling, F. Imaging of pH in vivo using hyperpolarized 13C-labelled zymonic acid. *Nat. Commun.* **2017**, *8*, 15126.

(51) Tomita, T.; Kato, M.; Hiratsuka, S. Regulation of Vascular Permeability in Cancer Metastasis. *Cancer Sci.* **2021**, *112*, 2966−2974.

(52) Magniont, C.; Escadeillas, G.; Oms-Multon, C.; De Caro, P. The Benefits of Incorporating Glycerol Carbonate into an Innovative Pozzolanic Matrix. *Cem. Concr. Res.* **2010**, *40*, 1072−1080.

(53) Schloerb, P. R.; Friis-Hansen, B. J.; Edelman, I. S.; Solomon, A. K.; Moore, F. D. The Measurement of Total Body Water in the Human Subject by Deuterium Oxide Dilution; with a Consideration of the Dynamics of Deuterium Distribution. *J. Clin. Invest.* **1950**, *29*, 1296−1310.

(54) Kushner, D. J.; Baker, A.; Dunstall, T. G. Pharmacological Uses and Perspectives of Heavy Water and Deuterated Compounds. *Can. J. Physiol. Pharmacol.* **1999**, *77*, 79−88.

(55) Korenchan, D. E.; Gordon, J. W.; Subramaniam, S.; Sriram, R.; Baligand, C.; VanCriekinge, M.; Bok, R.; Vigneron, D. B.; Wilson, D. M.; Larson, P. E. Z.; et al. Using Bidirectional Chemical Exchange for Improved Hyperpolarized [13 C]Bicarbonate PH Imaging. *Magn. Reson. Med.* **2019**, *82*, 959−972.

(56) Nguyen, H. M.; Vessella, R. L.; Morrissey, C.; Brown, L. G.; Coleman, I. M.; Higano, C. S.; Mostaghel, E. A.; Zhang, X.; True, L. D.; Lam, H.-M.; et al. LuCaP Prostate Cancer Patient-Derived Xenografts Reflect the Molecular Heterogeneity of Advanced Disease an–d Serve as Models for Evaluating Cancer Therapeutics. *Prostate* **2017**, *77*, 654−671.

(57) THAM solution - Trromethanmine Injection. https://www.accessdata.fda.gov/drugsatfda_docs/label/2006/013025s040lbl.pdf (accessed May 16, 2022).

(58) Mason, R. P. Transmembrane PH Gradients In Vivo: Measurements Using Fluorinated Vitamin 86 Derivatives*. *CMC* **1999**, *6*, 481−499.

(59) Gillies, R. J.; Liu, Z.; Bhujwalla, Z. 31P-MRS Measurements of Extracellular PH of Tumors Using 3-Aminopropylphosphonate. *Am. J. Physiol.: Cell Physiol.* **1994**, *267*, C195−203.

(60) Beauregard, D. A.; Parker, D.; Brindle, K. M. Relaxation-Based Mapping of Tumour PH. *Proc. Int. Soc. Magn. Reson. Med.* **1998**, *6*, 53.

(61) Raghunand, N.; Zhang, S.; Sherry, A. D.; Gillies, R. J. In Vivo Magnetic Resonance Imaging of Tissue PH Using a Novel PH-Sensitive Contrast Agent, GdDOTA-4AmP. *Acad. Radiol.* **2002**, *9* (Suppl 2), S481−S483.

(62) Ward, K. M.; Balaban, R. S. Determination of PH Using Water Protons and Chemical Exchange Dependent Saturation Transfer (CEST). *Magn. Reson. Med.* **2000**, *44*, 799−802.

(63) Wu, Y.; Zhou, I. Y.; Igarashi, T.; Longo, D. L.; Aime, S.; Sun, P. Z. A Generalized Ratiometric Chemical Exchange Saturation Transfer (CEST) MRI Approach for Mapping Renal PH Using Iopamidol. *Magn. Reson. Med.* **2018**, *79*, 1553−1558.